SURFACE CHEMISTRY

Nanoscale coherent phonon spectroscopy

Shuyi Liu[1], Adnan Hammud[2], Ikutaro Hamada[3], Martin Wolf[1], Melanie Müller[1]*, Takashi Kumagai[1,4]*

Coherent phonon spectroscopy can provide microscopic insight into ultrafast lattice dynamics and its coupling to other degrees of freedom under nonequilibrium conditions. Ultrafast optical spectroscopy is a well-established method to study coherent phonons, but the diffraction limit has hampered observing their local dynamics directly. Here, we demonstrate nanoscale coherent phonon spectroscopy using ultrafast laser–induced scanning tunneling microscopy in a plasmonic junction. Coherent phonons are locally excited in ultrathin zinc oxide films by the tightly confined plasmonic field and are probed via the photoinduced tunneling current through an electronic resonance of the zinc oxide film. Concurrently performed tip-enhanced Raman spectroscopy allows us to identify the involved phonon modes. In contrast to the Raman spectra, the phonon dynamics observed in coherent phonon spectroscopy exhibit strong nanoscale spatial variations that are correlated with the distribution of the electronic local density of states resolved by scanning tunneling spectroscopy.

INTRODUCTION

Tracking the time evolution of coherent lattice vibrations can provide valuable insight into the mutual coupling between electronic and structural degrees of freedom in condensed matter. Collective oscillations of atoms can be induced by ultrafast excitation with a laser pulse whose duration is shorter than the period of nuclear vibration. Coherent phonons (CPs) can be observed in various ways, for example, via their coupling to the electronic structure of the sample as used in optical spectroscopy and time-resolved photoelectron spectroscopy (*1*) or directly via the lattice response using time-resolved diffraction techniques (*2*, *3*). CPs have been investigated in a wide range of materials including metals (*4*), semimetals (*5*, *6*), semiconductors (*7*–*9*), oxides (*10*–*12*), strongly correlated materials (*13*, *14*), carbon materials (*15*, *16*), molecular crystals (*17*), and for atoms/molecules adsorbed on surfaces (*18*). On femtosecond time scales, the electronic and phononic systems after impulsive excitation are not in equilibrium, and the dynamics of CPs evolve through electron-phonon or phonon-phonon scattering. It has been shown recently that CPs can also be used to control the rearrangement of atoms during a photoinduced phase transition (*3*). The dynamics of CPs will be sensitive to nanoscale perturbations of the local lattice potential, e.g., originating from point defects in a crystal (*19*). However, the real-space observation of CPs approaching atomic length scales remains a challenging task.

To attain ultrafast spectroscopy at the atomic scale, continuous efforts have been devoted to combine scanning tunneling microscopy (STM) with ultrashort laser excitation in the past decades (*20*–*26*). More recently, coupling phase-stable, single-cycle terahertz or near-infrared (NIR) pulses to the STM junction has allowed to trace ultrafast charge carrier dynamics (*27*–*29*), plasmon dynamics (*30*), and electronic coherences (*31*, *32*) with subcycle temporal resolution. In addition, it was demonstrated that ultrafast STM can probe coherent vibrational motion of single molecules with angstrom spatial and femtosecond temporal resolution (*26*, *29*, *33*). More recently, it was demonstrated that coherent acoustic phonons can be launched in a thin metal film by local femtosecond Coulomb forces using a terahertz-gated STM (*34*). However, ultrafast photoexcitation and real-time observation of optically excited CPs on the nanoscale remain to be demonstrated. Here, we show nanoscale coherent phonon spectroscopy (CPS) on ultrathin zinc oxide (ZnO) films by coupling ultrashort NIR laser pulses into a plasmonic STM junction. The strong confinement of the plasmonic field enables us to locally excite and probe the ultrafast lattice dynamics of few-monolayer (ML) ZnO films with ~2-nm and ~10-fs spatiotemporal resolution. Furthermore, the combination of nanoscale CPS with scanning tunneling spectroscopy (STS) and tip-enhanced Raman spectroscopy (TERS) allows us to correlate the local equilibrium electronic structure and phonon modes concurrently with the CPs excited under nonequilibrium conditions.

RESULTS

Our approach to probing local ultrafast dynamics with photoinduced STM is based on femtosecond laser excitation of a plasmonic tunneling junction as illustrated in Fig. 1A. The STM junction consists of the clean Ag(111) surface and a nanoscopically sharp Ag tip fabricated by focused ion beam milling (*35*). The junction is illuminated by two collinear NIR pulses of 10-fs duration at a center wavelength of 780 nm and a repetition rate of 80 MHz. The pulse pair is created by separating a laser beam using a balanced-dispersion Michelson interferometer with variable delay in one arm. Both pulses are linearly polarized along the tip axis. The resulting highly confined plasmonic field enables optical excitation in the STM junction at a scale of a few nanometers (*36*) and generates an optically induced tunneling current at low incident laser power densities (P_{inc} < 0.2 mW/μm^2, which corresponds to the laser power of <2 mW incident into the STM junction). This low incident power is highly beneficial for keeping the junction stable and minimizing photoinduced thermal effects (*23*). The detected STM current (I_{STM}) under illumination is the sum of the static tunneling current (I_{DC}) induced by the applied DC bias (V_{bias}) and the photoinduced current (I_{photo}). The I_{photo} originates from transfer of photoexcited electrons across the junction

[1]Department of Physical Chemistry, Fritz Haber Institute of the Max Planck Society, Faradayweg 4-6, 14195 Berlin, Germany. [2]Department of Inorganic Chemistry, Fritz Haber Institute of the Max Planck Society, Faradayweg 4-6, 14195 Berlin, Germany. [3]Department of Precision Engineering, Graduate School of Engineering, Osaka University, 2-1 Yamada-Oka, Suita, Osaka 565-0871, Japan. [4]Center for Mesoscopic Sciences, Institute for Molecular Science, Okazaki 444-8585, Japan.
*Corresponding author. Email: m.mueller@fhi-berlin.mpg.de (M.M.); kuma@ims.ac.jp (T.K.)

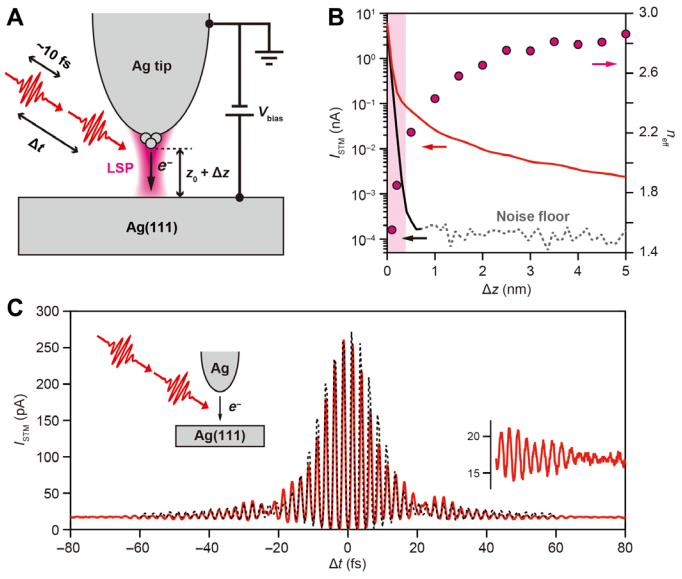

Fig. 1. Ultrashort pulsed laser–induced STM in a plasmonic junction. (**A**) Schematic of the experiment. (**B**) I_{STM}–Δz curves recorded with (red) and without (black) illumination. $\Delta z = 0$ corresponds to the STM set point of $V_{bias} = 2$ V and $I_{STM} = 6$ nA at $P_{inc} = 0.16$ mW/μm^2. The red circles show the n_{eff} extracted from the peak-to-baseline ratio r of the IAC trace using the formula $n_{eff} = [\log_2(r) + 1]/2$. (**C**) IAC trace of the photocurrent from the tip recorded for the Ag tip–Ag(111) junction at $V_{bias} = 2$ V with fixed tip height at $\Delta z = 1$ nm. The dashed line indicates the fitting result using Eqs. 1 and 2. The inset is the magnified IAC trace after a delay time of 40 fs.

either above the vacuum barrier or via photoassisted tunneling (*37*). With the excitation wavelength at 780 nm, one-, two- and three-photon–excited electrons gain an excess energy of ~1.6, ~3.2, and ~ 4.8 eV, respectively. Because the work function of the Ag surface is 4.2 to 4.7 eV (*38*), the one- and two-photon processes result in the I_{photo} through photoassisted tunneling, whereas the three-photon process can lead to the I_{photo} through over-barrier emission. The proportion of electrons that are emitted above or tunnel through the barrier depends on the barrier width (i.e., tip–surface distance). Electron tunneling becomes dominant at a small tip–surface distance where the tunneling probability is large. Under illumination, the I_{photo} consists of electrons transferred from both tip and surface, but the electron transfer from the tip (surface) can be suppressed by applying a negative (positive) bias to the surface. The exact magnitude of the negative (positive) bias required to suppress the I_{photo} contribution from the tip (surface) depends on the incident laser power, the tip–surface distance, and the tip conditions (plasmon enhancement).

To characterize the plasmonic response of the junction, we measure I_{photo} from the tip to the surface at a positive sample bias. The relative contribution from I_{DC} and I_{photo} can be assessed by recording I_{STM} as a function of the relative tip–surface distance (Δz) with and without illumination (Fig. 1B). Here, $\Delta z = 0$ corresponds to the tip–surface distance given by the STM set-point of $V_{bias} = 2$ V and $I_{STM} = 5$ nA. At $\Delta z < 0.1$ nm, the total current (I_{STM}) is dominated by the I_{DC}. The I_{photo} mainly contributes to the I_{STM} at $\Delta z > 0.3$ nm and extends more than 5 nm outside the tunneling regime (red curve in Fig. 1B). Figure 1C shows the I_{photo} recorded for the Ag tip–Ag(111) junction as a function of the time delay (Δt) between the two NIR pulses, yielding the interferometric autocorrelation (IAC) of the I_{photo}. The data are recorded at $\Delta z = 1$ nm outside the tunneling regime, and the plasmonically enhanced interferometric I_{photo} can be detected at a sufficient signal-to-noise ratio without lock-in detection methods. The photothermal modulation (noise) of the junction during the IAC measurement is estimated to be less than 0.05 nm at $P_{inc} = 0.12$ mW/μm^2 (see fig. S1), which does not significantly affect the I_{photo} because of the shallow I_{STM}–Δz slope in the used distance range. Thus, the contribution from thermal expansion is almost negligible in the IAC measurement when it is recorded in the photoinduced tunneling regime, in which the I_{photo} is dominant. The IAC trace measured for the Ag tip–Ag(111) junction can be fitted by

$$I_{IAC}(\Delta t) \propto \int_{-\infty}^{+\infty} |\,(E_{pl}(t) + E_{pl}(t-\Delta t))\,|^{2n_{eff}}\, dt \qquad (1)$$

where E_{pl} is the plasmonic field and n_{eff} is the effective nonlinearity of the photoinduced process. The noninstantaneous plasmonic response of the Ag tip–Ag(111) junction contributes to the IAC trace, leading to broadening of the central envelope and the appearance of satellite tails extending to tens of femtoseconds (inset to Fig. 1C) (*39*). We approximate the plasmon dynamics by a damped harmonic oscillator driven by the laser pulse field $E(t)$, resulting in the plasmon-enhanced field

$$E_{pl}(t) \propto \int_{-\infty}^{t} \frac{1}{\omega_{pl}} E(t') \exp\left(-\frac{t-t'}{\tau_{pl}}\right) \sin(\omega_{pl}(t-t'))\, dt' \qquad (2)$$

where $E(t') = \mathrm{sech}\left(\frac{t'}{\tau}\right)\sin(\omega t')$ is the electric field of the individual laser pulses with a hyperbolic secant shape of duration τ (full width at half maximum) and τ_{pl} and ω_{pl} are the decoherence time and the resonance frequency of the plasmon, respectively. The fitting analysis can reproduce the IAC trace reasonably well (black dashed line in Fig. 1C) and yields τ_{pl}~25 fs, ω_{pl}~ 421.6 THz (corresponding to a photon wavelength of 711 nm). This dephasing time is consistent with the reported dephasing time of Ag nanoparticle plasmons (*40*, *41*). To clarify the contribution from the localized surface plasmon (LSP), we record an IAC trace for nonlinear photoemission from a Cu(111) surface that exhibits a much weaker plasmonic response. The result reveals a negligible plasmon response, and the IAC trace can be used to evaluate the pulse duration at the junction (see fig. S2). We further evaluate the effective nonlinearity n_{eff} of the I_{photo} from the peak-to-baseline ratio r of the IAC trace, revealing that the n_{eff} decreases from 2.8 to 1.6 as Δz decreases (Fig. 1B). This observation evidences the increasing contribution of lower-order processes due to photoassisted tunneling at short tip–surface distances.

The femtosecond time resolution achievable with ultrafast photoinduced STM allows us to trace ultrafast dynamics at surfaces in real time and in real space. We apply the above measurement scheme to locally excite and probe ultrafast lattice dynamics in ultrathin ZnO films epitaxially grown on the Ag(111) surface (*42*). A coherent lattice oscillation was previously proposed in femtosecond laser-coupled STM (*24*), but it has remained uncorroborated. Figure 2A illustrates the experiment, which is the same setup as depicted in Fig. 1 but with a negative V_{bias} applied to the sample to suppress the transfer of photoexcited electrons from the tip. Figure 2B compares the I_{STM}–Δz curves under femtosecond laser illumination recorded over the bare Ag(111) surface and over the regions of 2- and 3-ML ZnO (hereafter denoted by 2-ML and 3-ML ZnO). Note that the current is given by the absolute value and the electrons flow from the surface to the tip. The simulated structure of 2- and 3-ML ZnO is reported

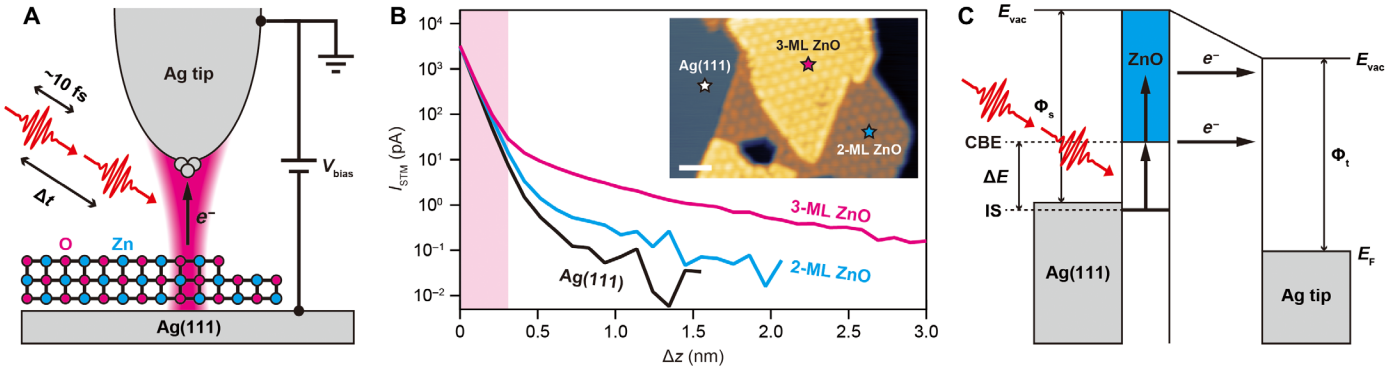

Fig. 2. Photoinduced resonant electron tunneling from the ultrathin ZnO films. (**A**) Schematic of the experiment. (**B**) I_{STM}–Δz curves recorded over the bare Ag(111) surface, 2-ML, and 3-ML ZnO, respectively. The measurement locations are indicated by the stars in the inset STM image (scale bar, 5 nm). $\Delta z = 0$ corresponds to the tip–surface distance given by the STM set point of $V_{bias} = -2$ V and $I_{STM} = 3$ nA at $P_{inc} = 0.08$ mW/μm^2. Note that the current is given by the absolute value and the electrons flow from the surface to the tip. (**C**) Schematic energy diagram. $\Phi_{s/t}$, work function of surface/tip; E_{vac}, vacuum level. The vertical and horizontal arrows indicate electronic excitation and electron transfer, respectively.

in (*36*) and in fig. S3, respectively. We found that the I_{photo} is larger for 3-ML ZnO by one order of magnitude compared to the other two cases. The large I_{photo} from 3-ML ZnO can be explained by resonant photoassisted tunneling, which is absent for 2-ML ZnO and the Ag(111) surface. Figure 2C depicts the schematic energy diagram of the Ag tip–vacuum–ZnO–Ag(111) junction. The position of the conduction band edge (CBE) of the ultrathin ZnO films depends on the film thickness, and its onset can be observed in STS at ~1.8 and ~1.4 eV above the Fermi level (E_F) for 2- and 3-ML ZnO, respectively (*42*). Furthermore, the interface state (IS) between the ZnO film and the Ag(111) surface is located at ~0.2 eV below E_F, originating from the Shockley surface state of Ag(111) (*42*). In contrast to 2-ML ZnO, the transition from the IS to the CBE is resonant with the excitation wavelength (780 nm) for 3-ML ZnO, resulting in a much larger I_{photo}. We also confirm that the local work function of the surface (Φ_s) is not primarily related to the transfer of photoexcited electrons in the junction (see fig. S4).

The resonant electronic excitation of 3-ML ZnO yields the enhanced I_{photo} and allows us to observe the CPs excited impulsively via the resonant optical excitation. Figure 3A shows representative IAC of the I_{photo} recorded at three different locations on 3-ML ZnO with Δz = 0.5 nm in the regime where I_{DC} is negligible. In addition to the coherent electronic center part of the IAC including the response of the LSP (<25 fs), all traces exhibit pronounced oscillations extending up to ~1.5 ps, and their detailed profiles differ at the three locations. In the Fourier transform (FT) of the IAC traces (Fig. 3B), several peaks appear in the range of 7.5 to 21.0 THz. The peak positions in the IAC-FT spectra are consistent with the phonon modes observed in TERS measured at the same position (Fig. 3C). TERS provides equilibrium phonon spectra in the frequency domain with ultrahigh spatial resolution reaching ~1 nm (*36*). In Fig. 3C, the bands at 250 to 460 cm^{-1} and 470 to 700 cm^{-1} can be assigned to the out-of-plane and in-plane phonon modes of the ZnO film, respectively (*36*, *43*). Therefore, we conclude that the long-lasting oscillations observed in the IAC traces result from CPs of 3-ML ZnO. In the out-of-plane and in-plane modes, atoms in the ZnO film are mainly displaced perpendicular and parallel to the surface, respectively. The out-of-plane modes will slightly change the tip–surface distance, which, in principle, can modify the tunneling probability (i.e., I_{photo}). However, this should not contribute to the observed modulation of the I_{photo}. The coherent lattice displacement is estimated to be 10^{-4} to 10^{-3} nm (*44*, *45*), which is much smaller than the tip–surface distance (~1 nm) used in the IAC measurements. As discussed above, at the distance of the IAC measurement, the slope of the I_{photo}-Δz curve is rather small; hence, a CP-induced displacement of the atoms cannot result in a measurable change of I_{STM}. The negligible contribution is also corroborated by the fact that the amplitude of the in-plane modes is larger than the out-of-plane modes in some cases. Instead, we deduce that the CPs modulate the electronic structure of the ZnO film, eventually modifying the magnitude of the I_{photo} through a change in the transition probability from IS to CB. The local work function may also be modulated by the CPs, which could affect the apparent barrier height and, thus, the tunneling probability. However, because, at a positive bias, the I_{photo} caused by electron transfer from the tip is not modulated by the CPs, the local work function change plays a minor role. The involved phonon modes are further analyzed by fitting the IAC trace with a damped harmonic oscillator model. Assuming that the phonon-induced modulation of the I_{photo} is, in first-order approximation, linearly proportional to the phonon amplitude, we can fit the IAC traces in Fig. 3A to a model of multiple damped oscillators

$$I_{IAC} = \sum_i A_i \sin(2\pi\omega_i \Delta t + \varphi_i)\, e^{-\Delta t/\tau_i} + I_0 \quad (3)$$

where the ith damped oscillator is characterized by the initial amplitude A_i, the frequency ω_i, the initial phase φ_i, and the damping time τ_i. We deduce the phonon frequencies that are involved in the IAC trace based on the analysis of the IAC-FT and TERS spectra in Fig. 3 (B and C). The fitting results (the black dashed curves in Fig. 3A) reproduce fairly well the IAC trace using five phonon modes at frequencies of 300, 340, 400, 433, and 530 cm^{-1}. Note that there is one measurably different peak at 340 cm^{-1} in the FT spectra instead of 360 cm^{-1} in TERS [these peaks are highlighted by vertical black lines in Fig. 3 (B and C)]. The fitting procedure and parameters for all phonon modes are described in the Supplementary Materials, showing that the values of A_i, φ_i, and τ_i largely depend on the measurement site.

The observed spatial variation of the IAC trace should be associated with the underlying mechanisms of the CP excitation and relaxation. To rationalize the CP excitation, two key processes have

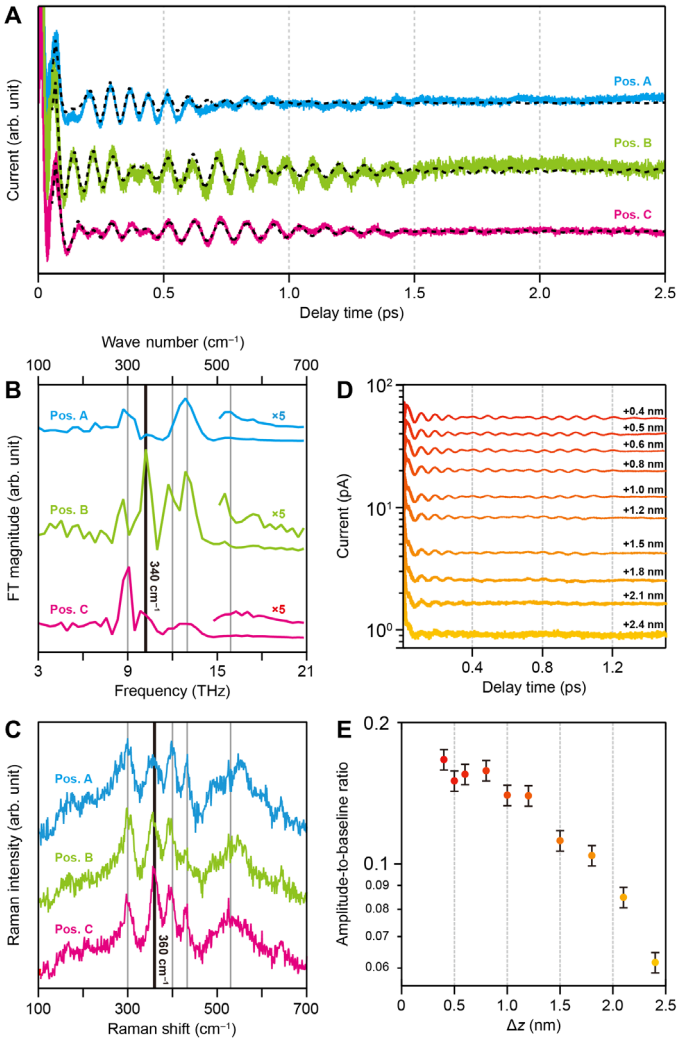

Fig. 3. CPs measured in ultrathin 3-ML ZnO. (**A**) IAC traces measured over different locations over 3-ML ZnO (set point: $V_{bias} = -4$ V, $I_{STM} = 2$ nA, $\Delta z = 0.5$ nm, $P_{inc} = 0.08$ mW/μm^2). The dashed lines are fits obtained using Eq. 3 with the parameters provided in table S1. (**B**) FT spectra obtained from the IAC traces in (A). (**C**) TERS spectra recorded with a narrowband continuous wave laser at 780 nm ($P_{inc} = 0.8$ mW/μm^2) at a set point of $V_{bias} = 50$ mV and $I_{STM} = 3$ nA. The vertical solid lines in (B) and (C) indicate the frequencies used for the fitting analysis in (A). (**D**) IAC traces recorded over 3-ML ZnO at different Δz ($\Delta z = 0$ corresponds to the tip–surface distance given by the STM set point of $V_{bias} = -1$ V, $I_{STM} = 3$ nA, $P_{inc} = 0.08$ mW/μm^2). (**E**) Semi-log plot of the amplitude-to-baseline ratio of the traces in (D) as a function of Δz. Note that the current is given by the absolute value and the electrons flow from the surface to the tip.

been discussed, namely displacive excitation of CPs (DECP) (*46*) and impulsive stimulated Raman scattering (ISRS) (*47*, *48*). The DECP mechanism involves real electronic transitions that create an excited state population. The corresponding rearrangement of charges leads to a displaced potential energy surface, which can eventually drive coherent lattice motion. In contrast, ISRS drives Raman active modes via a virtual excitation, which is typically the operating mechanism in transparent media. In the present case, the pronounced discrepancy in the spectral distributions between the frequency- and time-domain measurements, i.e., the frequency at 340 cm^{-1} observed in the IAC-FT spectra in Fig. 3B being different from the TERS spectra, indicates that resonant Raman scattering cannot be a dominant mechanism responsible for CP generation in the ZnO film. As the excitation wavelength of 780 nm is resonant with the electronic transition between the IS and the CBE of 3-ML ZnO, we believe that the DECP mechanism is a major driving force. DECP and ISRS are often distinguished by the initial phonon phase, which are zero for the ISRS mechanism under nonresonant conditions. The phases (φ_i) in Eq. 3 are all nonzero (see table S1). The original DECP theory predicts $\varphi_i = \frac{\pi}{2}$ when the lifetime of a coupled electronically excited state is much longer than the period of the coherent lattice oscillation (*49*). However, all φ_i obtained from the fitting analysis in Fig. 3A largely deviate from $\frac{\pi}{2}$ (table S1). This could be explained by a short lifetime of the resonantly excited charge carriers compared to that of the coherent lattice oscillation (*49*). The absence of an (incoherent) electronic decay in the IAC traces implies that the lifetime of the excited electrons is shorter than the plasmon dephasing (i.e. <25 fs). In this case, the resulting displacive force becomes more impulsive, thus yielding $\varphi_i \neq \frac{\pi}{2}$ (*49*, *50*). The short electron lifetime could be explained by fast relaxation of the excited state(s) into the Ag substrate and/or by the nature of the highly localized excitation inside the plasmonic field, for which lateral transport of excited electrons out of the excitation volume could effectively reduce the lifetime of the locally excited charge density. We note that the CPs are excited by the local electromagnetic field enhanced by the LSP in the STM junction, which differs significantly from far-field excitation. The strong field confinement (to Δx) leads to momentum uncertainty, which is given by $\Delta k \sim \pi/\Delta x$ in the optical excitation, which could relax the momentum conservation required in far-field optical excitation (*51*, *52*). The momentum uncertainty could contribute to the electronic transition and result in excitation of phonons away from the Γ point.

In the DECP model, the amplitude of CPs is assumed to be linearly proportional to the excited charge density (*46*, *49*). We thus examine how the localized plasmonic field will affect CP excitation. According to previous TERS measurements (*53*), the LSP is exponentially enhanced as the tip–surface distance is reduced. Figure 3D shows the Δz-dependent IAC traces obtained on 3-ML ZnO. The shape of the IAC traces is independent of Δz; thus, the CP dynamics are not noticeably modified by the change of the LSP enhancement. The amplitude of the CPs can be evaluated by analyzing the transient photocurrent change, i.e., the ratio between the coherent oscillation amplitude and the IAC baseline current. Provided I_{DC} is negligible, and the relative oscillation amplitude of the IAC induced by the CPs is approximately proportional to the nuclear displacement (ΔQ); thus

$$\Delta Q \propto \frac{I_{dis} - I_{eq}}{I_{eq}} = \frac{2(I_{IAC} - I_0)}{I_0} \quad (4)$$

where $I_{IAC} = I_{dis} + I_{eq}$, I_{dis} is the photocurrent from the probe pulse in the presence of the CPs, and $I_{eq} = \frac{I_0}{2}$ is the photocurrent from a single pulse at equilibrium lattice positions. As plotted in Fig. 3E, we found that ΔQ increases as Δz is decreased for $\Delta z > 1$ nm, which is explained by the increased LSP field strength with decreasing the tip–surface distance. However, ΔQ saturates for $\Delta z < 1$ nm, implying that the phonon amplitude is saturated when the local field becomes very strong. At extremely small cavity distances, the LSP will be damped because of quantum mechanical effects (*54*, *55*). As previously reported (*53*), damping is expected to occur at Ag tip–Ag(111)

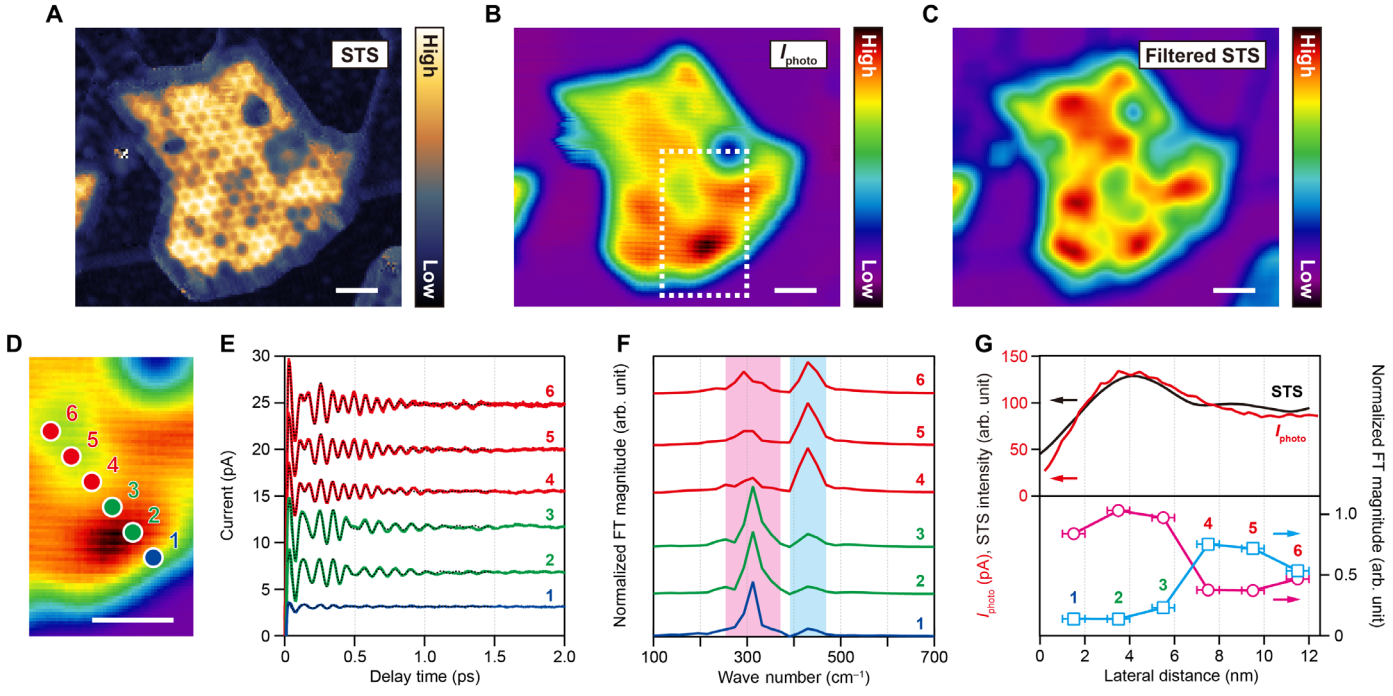

Fig. 4. Nanoscale CPS. (**A**) STS map (V_{bias} = 1.5 V, I_{STM} = 0.3 nA), representing the LDOS of the CBE of 3-ML ZnO. (**B**) I_{photo} map recorded over the same 3-ML ZnO island in constant height mode (Δz = 0 corresponds to the tip–surface distance given by the STM set point of V_{bias} = −3 V, I_{STM} = 4 nA, Δz = 0.5 nm, P_{inc} = 0.16 mW/μm^2). (**C**) Blurred STS map of (A) using a mean filter with the diameter of 4 nm. (**D**) The region of interest is indicated by the white dashed box in (B). Scale bars, 5 nm (A to D). (**E**) IAC traces at different positions marked in the enlarged I_{photo} image in (D). Note that the current is given by the absolute value, and the electrons flow from the surface to the tip. The dashed lines are the fitting curves, and the parameters are provided in table S2. (**F**) Corresponding FT spectra of the IAC traces in (E). The FT magnitude is normalized with respect to the IAC baseline. (**G**) Lateral distance dependence of the filtered STS intensity, I_{photo}, and the FT peak magnitude along the line scan in (E). The magenta and cyan markers in the bottom panel are the FT magnitudes integrated over the range of 254 to 371 cm^{-1} and 391 to 469 cm^{-1}, respectively, as shaded in (F).

surface distances smaller than ~0.5 nm, at which the tip is nearly in atomic contact to the surface of 2-ML ZnO film. However, all the IAC measurements are performed at a distance of ~1 nm; hence, the ΔQ saturation cannot be explained by attenuation of the LSP. We speculate that the saturating behavior may be related to limited carrier generation due to the strong spatiotemporal confinement of the exciting plasmon field. Above a certain strength of the extremely localized and enhanced field, the locally excited charge density might be saturated because of Coulomb repulsion.

The generation of CPs via optical excitation is fundamentally associated with the electronic structure of the sample. The versatility of ultrafast STM enables the concurrent observation of local femtosecond dynamics and equilibrium electronic states. Figure 4A shows an STS intensity map recorded at V_{bias} = 1.5 V without laser illumination, representing the distribution of the local density of states (LDOS) of the CB of 3-ML ZnO. The contrast modulation inside the 3-ML ZnO arises from inhomogeneities originating from atomistic defects in the film (*56*). Figure 4B displays the corresponding I_{photo} map recorded at Δz = 0.5 nm, exhibiting pronounced nanoscale variations. However, the spatial resolution of the I_{photo} map is lower than that of the STS map and will be determined by the lateral size of the plasmonic field in the junction (*37*). This assumption can be verified in the artificially "blurred" STS map using a mean filter with the diameter of 4 nm that accounts for the field localization (the size of the plasmonic field). The blurred STS map (Fig. 4C) is indeed very similar to the I_{photo} map (Fig. 4B), indicating that the plasmonic field is confined to ~4 nm underneath the tip and further corroborating that the I_{photo} is enhanced through the electronic resonance. The I_{photo} is larger at positions of higher LDOS because of a larger transition matrix for the photoexcitation. The I_{photo} and blurred STS maps exhibit "domains" in their contrast on a length scale of 2 to 8 nm. Figure 4 (D to F) display the IAC traces and corresponding FT spectra recorded across the different domains with a 2-nm interval. Whereas the IAC traces do not change significantly inside each domain, an abrupt change of the beating pattern occurs within a 2-nm length scale between neighboring domains. In the FT spectra, this is manifested as a significant change in the relative peak intensities of the involved phonon modes (Fig. 4F; see also table S2, which lists the fitting parameters of the IAC traces in Fig. 4D). As can be seen in Fig. 4G, the change in the relative peak intensities (and in the fitting parameters in table S2) correlates with the spatial variation of the STS intensity and I_{photo}.

The dephasing of CPs can involve complex contributions, such as anharmonic coupling between phonon modes, which is dominant in bulk ZnO (*12*). However, the phonon dephasing time in bulk ZnO is estimated to be several picoseconds, thus much longer than the τ_i obtained in the present case. Therefore, anharmonic coupling within 3-ML ZnO should not be a major damping channel. However, phonon scattering at atomistic defects is reported as a damping channel of CPs (*19*), which potentially contributes to the dephasing process of the CPs. For adsorbates on metal surfaces, multiple channels may contribute simultaneously to the vibrational damping, namely, interadsorbate interactions (*57*), electron–hole pair (EHP) excitation in a metal (*58*), anharmonic coupling to surface

phonons (*59*), and hot-electron scattering (*60*). Damping through hot-electron scattering can be excluded by the Δz-dependence of the IAC traces in Fig. 3E. At smaller tip–surface distances, hot electrons will be excited more efficiently because of the increased LSP field in the junction, but the observed CP dynamics are not affected. The contribution from EHP excitation and anharmonic coupling to surface phonons depends on the interaction between the adsorbate and the surface (*61*). Because the ZnO film is physisorbed onto the Ag(111) surface, these channels may not be dominant. The locally excited CPs in the ZnO film may efficiently couple to the surrounding lattice because they have the same phonon modes (the phonon frequency is not influenced by the inhomogeneity as evidenced by the TERS spectra in Fig. 3C). However, to gain further insight into the complex phonon dynamics in the ZnO film is challenging in the present work. Polarization-dependent measurements, which are commonly used to distinguish CP modes with different symmetry, are not straightforward to implement in the present case because of the nontrivial polarization of the tightly confined plasmonic near field. We expect that more insight into the underlying mechanism can be gained by variation of the resonant excitation condition, e.g., by using a tunable wavelength femtosecond laser source.

DISCUSSION

We demonstrated the capability of ultrasfast NIR laser-induced STM to resolve the spatial inhomogeneity of ultrafast lattice dynamics in ultrathin ZnO films with ~2-nm and ~10-fs spatiotemporal resolution. We exploited the strong confinement and enhancement of the LSP in the STM junction to obtain spatially localized ultrafast photocurrents at very low excitation power. The LSP field allowed us to operate the photoinduced STM outside the normal tunneling regime while maintaining a high spatial resolution that is determined by the localization of the photoassisted tunneling current. This operation mode largely mitigated the thermal effects that usually disturb the measurement and interpretation of two-pulse autocorrelation experiments performed in the femtosecond laser-coupled STM. Furthermore, resonant optical excitation of photoassisted tunneling channels via the transition from the IS to the CB within the ZnO film yields sufficient photoinduced current to detect the ultrafast coherent lattice vibrations. The resonant excitation condition, together with the observed discrepancies between the TERS and time-domain spectra of CPs, indicated that the DECP mechanism is involved in the CP generation in 3-ML ZnO films. The concurrent real-space observation of the local electronic structure and equilibrium phonon modes by STS and TERS is a unique capability of STM and enables to investigate the complex correlation between ultrafast dynamics of electron–phonon and phonon–phonon coupling.

The presented experimental concept for nanoscale CPS can be applied to investigate the excited state dynamics and the interplay between electronic and phononic degrees of freedom at photoexcited surfaces on length scales approaching a few unit cells. To extend the approach to other sample systems and to control the resonant condition in the excitation process, it will be beneficial to combine wavelength-tunable pulsed lasers with a broadband LSP resonance in the STM junction. We expect that higher spatial resolution approaching the atomic scale can be achieved by using plasmonic picocavities (*62*), confining the plasmonic near-field down to a few atoms (*63*, *64*). Operating at closer tip–surface distances to increase spatial resolution will remain a significant challenge due to the remaining small but unavoidable thermal effects. To overcome these issues, lock-in detection of the laser-induced tunneling current without amplitude modulation (*31*) or combination with terahertz-gated STM might be promising approaches. We envision that real-time and real-space observation of ultrafast coherent lattice dynamics using ultrafast photoinduced STM may pave the way for studying the coupling of fundamental degrees of freedom in solids—lattice, charge, orbital, and spin—on the atomic scale.

MATERIALS AND METHODS

All experiments were performed inside an ultrahigh vacuum (UHV) (base pressure of $<5 \times 10^{-10}$ mbar) chamber equipped with a low-temperature STM system from UNISOKU Ltd. (modified USM-1400) that is operated with Nanonis SPM Controller from SPECS GmbH. The bias voltage (V_{bias}) was applied to the sample, and the tip was grounded. The I_{STM} was collected from the tip through a current amplifier from FEMTO Messtechnik GmbH (DLPCA-200). The Ag tips are prepared in a two-step process. First, an Ag wire was chemically etched to obtain a sharp tip, which was then further sharpened by focused ion beam milling to yield a nanoscopically sharp plasmonic tip as detailed in (*35*).

The STM junction was illuminated by a titanium-sapphire laser oscillator from Laser Quantum (Venteon Pulse One), which provides 10-fs laser pulses at 780-nm center wavelength and 80-MHz repetition rate. A spectral phase interferometry for direct electric-field reconstruction (SPIDER, APE GmbH) was used to measure the duration of the laser pulse at a reference beam path with identical dispersion outside UHV. To couple with the low-temperature STM, the laser beam enters the UHV chamber through a fused silica window. A chirped mirror pair is used for dispersion control and to precompensate the dispersion of the setup. The laser polarization was aligned along the tip axis (p-polarized). The beam is focused inside the UHV by a custom-designed parabolic mirror with a focal length of 8 mm to ~3-μm spot size in the junction. The parabolic mirror was precisely aligned using piezo motors (Attocube GmbH) enabling three translational and two rotational motions. Collinear pairs of identical pulses are generated inside a dispersion-balanced Michelson interferometer. The laser power is equal in both interferometer arms, and before measurements, it was checked that the photocurrent from both arms is additive at large delays far away from temporal overlap of the two pulses. In the IAC measurements, the delay is controlled by a closed-loop piezo stage (PI-Hera) operated at 0.5- to 2-Hz scanning frequency, and the I_{STM} is time-averaged over several scanning cycles. The maximum scanning speed is thereby limited by the bandwidth of the preamplifier (1 kHz here) and the fastest frequency components that need to be resolved in the IAC trace.

TERS was measured using a narrow-band solid-state laser at 780 nm. The beam was focused by the same parabolic mirror as mentioned above. The Raman signal was collected in the back-scattering geometry and was detected outside of the UHV chamber with a grating spectrometer (AndorShamrock 303i) equipped with the back-illuminated charge-coupled device camera (Newton 970). The scattered light was separated by a beamsplitter (90:10) and filtered by a longpass filter before coupling to the spectrometer via an optical fiber.

The Ag(111) surface was first cleaned by repeated cycles of Ar^+ sputtering and annealing up to ~700 K. Ultrathin ZnO layers were

grown on the clean Ag(111) surface by reactive deposition method as described in (*65*).

SUPPLEMENTARY MATERIALS

Supplementary material for this article is available at https://science.org/doi/10.1126/sciadv.abq5682

REFERENCES AND NOTES

1. U. Bovensiepen, P. S. Kirchmann, Elementary relaxation processes investigated by femtosecond photoelectron spectroscopy of two-dimensional materials. *Laser Photonics Rev.* **6**, 589–606 (2012).
2. A. M. Lindenberg, I. Kang, S. L. Johnson, T. Missalla, P. A. Heimann, Z. Chang, J. Larsson, P. H. Bucksbaum, H. C. Kapteyn, H. A. Padmore, R. W. Lee, J. S. Wark, R. W. Falcone, Time-resolved x-ray diffraction from coherent phonons during a laser-induced phase transition. *Phys. Rev. Lett.* **84**, 111–114 (2000).
3. J. G. Horstmann, H. Böckmann, B. Wit, F. Kurtz, G. Storeck, C. Ropers, Coherent control of a surface structural phase transition. *Nature* **583**, 232–236 (2020).
4. M. Hase, K. Ishioka, J. Demsar, K. Ushida, M. Kitajima, Ultrafast dynamics of coherent optical phonons and nonequilibrium electrons in transition metals. *Phys. Rev. B* **72**, 189902 (2005).
5. M. Hase, K. Mizoguchi, H. Harima, S. Nakashima, M. Tani, K. Sakai, M. Hangyo, Optical control of coherent optical phonons in bismuth films. *Appl. Phys. Lett.* **69**, 2474–2476 (1996).
6. E. Papalazarou, J. Faure, J. Mauchain, M. Marsi, A. Taleb-Ibrahimi, I. Reshetnyak, A. van Roekeghem, I. Timrov, N. Vast, B. Arnaud, L. Perfetti, Coherent phonon coupling to individual bloch states in photoexcited bismuth. *Phys. Rev. Lett.* **108**, 256808 (2012).
7. T. Pfeifer, W. Kütt, H. Kurz, R. Scholz, Generation and detection of coherent optical phonons in germanium. *Phys. Rev. Lett.* **69**, 3248–3251 (1992).
8. M. Hase, M. Kitajima, A. M. Constantinescu, H. Petek, The birth of a quasiparticle in silicon observed in time–frequency space. *Nature* **426**, 51–54 (2003).
9. K. J. Yee, K. G. Lee, E. Oh, D. S. Kim, Coherent optical phonon oscillations in bulk GaN excited by far below the band gap photons. *Phys. Rev. Lett.* **88**, 105501 (2002).
10. I. H. Lee, K. J. Yee, K. G. Lee, E. Oh, D. S. Kim, Y. S. Lim, Coherent optical phonon mode oscillations in wurtzite ZnO excited by femtosecond pulses. *J. Appl. Phys.* **93**, 4939–4941 (2003).
11. C. Aku-Leh, J. Zhao, R. Merlin, J. Menendez, M. Cardona, Long-lived optical phonons in ZnO studied with impulsive stimulated Raman scattering. *Phys. Rev. B* **71**, 205211 (2005).
12. K. Ishioka, H. Petek, V. E. Kaydashev, E. M. Kaidashev, O. V. Misochko, Coherent optical phonons of ZnO under near resonant photoexcitation. *J. Phys. Condens. Matter* **22**, 465803 (2010).
13. L. Rettig, S. O. Mariager, A. Ferrer, S. Grübel, J. A. Johnson, J. Rittmann, T. Wolf, S. L. Johnson, G. Ingold, P. Beaud, U. Staub, Ultrafast structural dynamics of the Fe-pnictide parent compound $BaFe_2As_2$. *Phys. Rev. Lett.* **114**, 067402 (2015).
14. Y. Zhang, X. Shi, W. You, Z. Tao, Y. Zhong, F. C. Kabeer, P. Maldonado, P. M. Oppeneer, M. Bauer, K. Rossnagel, H. Kapteyn, M. Murnane, Coherent modulation of the electron temperature and electron–phonon couplings in a 2D material. *Proc. Natl. Acad. Sci. U.S.A.* **117**, 8788–8793 (2020).
15. K. Ishioka, M. Hase, M. Kitajima, L. Wirtz, A. Rubio, H. Petek, Ultrafast electron-phonon decoupling in graphite. *Phys. Rev. B* **77**, 121402 (2008).
16. A. Gambetta, C. Manzoni, E. Menna, M. Meneghetti, G. Cerullo, G. Lanzani, S. Tretiak, A. Piryatinski, A. Saxena, R. L. Martin, A. R. Bishop, Real-time observation of nonlinear coherent phonon dynamics in single-walled carbon nanotubes. *Nat. Phys.* **2**, 515–520 (2006).
17. H. Seiler, M. Krynski, D. Zahn, S. Hammer, Y. W. Windsor, T. Vasileiadis, J. Pflaum, R. Ernstorfer, M. Rossi, H. Schwoerer, Nuclear dynamics of singlet exciton fission in pentacene single crystals. *Sci. Adv.* **7**, eabg0869 (2021).
18. K. Watanabe, N. Takagi, Y. Matsumoto, Impulsive excitation of a vibrational mode of Cs on Pt(111). *Chem. Phys. Lett.* **366**, 606–610 (2002).
19. M. Hase, M. Kitajima, Interaction of coherent phonons with defects and elementary excitations. *J. Phys. Condens. Matter* **22**, 073201 (2010).
20. R. J. Hamers, Ultrafast time resolution in scanned probe microscopies. *Appl. Phys. Lett.* **57**, 2031–2033 (1990).
21. G. Nunes Jr., M. R. Freeman, Picosecond resolution in scanning tunneling microscopy. *Science* **262**, 1029–1032 (1993).
22. S. Weiss, D. F. Ogletree, D. Botkin, M. Salmeron, D. S. Chemla, Ultrafast scanning probe microscopy. *Appl. Phys. Lett.* **63**, 2567–2569 (1993).
23. V. Gerstner, A. Knoll, W. Pfeiffer, A. Thon, G. Gerber, Femtosecond laser assisted scanning tunneling microscopy. *J. Appl. Phys.* **88**, 4851–4859 (2000).
24. S. W. Wu, W. Ho, Two-photon-induced hot-electron transfer to a single molecule in a scanning tunneling microscope. *Phys. Rev. B* **82**, 085444 (2010).
25. Y. Terada, S. Yoshida, O. Takeuchi, H. Shigekawa, Real-space imaging of transient carrier dynamics by nanoscale pump–Probe microscopy. *Nat. Photonics* **4**, 869–874 (2010).
26. S. Li, S. Chen, J. Li, R. Wu, W. Ho, Joint space-time coherent vibration driven conformational transitions in a single molecule. *Phys. Rev. Lett.* **119**, 176002 (2017).
27. T. L. Cocker, V. Jelic, M. Gupta, S. J. Molesky, J. A. J. Burgess, G. D. L. Reyes, L. V. Titova, Y. Y. Tsui, M. R. Freeman, F. A. Hegmann, An ultrafast terahertz scanning tunnelling microscope. *Nat. Photonics* **7**, 620–625 (2013).
28. S. Yoshida, Y. Arashida, H. Hirori, T. Tachizaki, A. Taninaka, H. Ueno, O. Takeuchi, H. Shigekawa, Terahertz scanning tunneling microscopy for visualizing ultrafast electron motion in nanoscale potential variations. *ASC Photonics* **8**, 315–323 (2021).
29. T. L. Cocker, D. Peller, P. Yu, J. Repp, R. Huber, Tracking the ultrafast motion of a single molecule by femtosecond orbital imaging. *Nature* **539**, 263–267 (2016).
30. M. Garg, K. Kern, Attosecond coherent manipulation of electrons in tunneling microscopy. *Science* **367**, 411–415 (2020).
31. M. Garg, A. Martin-Jimenez, Y. Luo, K. Kern, Ultrafast photon-induced tunneling microscopy. *ACS Nano* **15**, 18071–18084 (2021).
32. M. Garg, A. Martin-Jimenez, M. Pisarra, Y. Luo, F. Martín, K. Kern, Real-space subfemtosecond imaging of quantum electronic coherences in molecules. *Nat. Photon.* **16**, 196–202 (2022).
33. L. Wang, Y. Xia, W. Ho, Atomic-scale quantum sensing based on the ultrafast coherence of an H_2 molecule in an STM cavity. *Science* **376**, 401–405 (2022).
34. S. Sheng, A.-C. Oeter, M. Abdo, K. Lichtenberg, M. Hentschel, S. Loth, Launching coherent acoustic phonon wave packets with local femtosecond coulomb forces. *Phys. Rev. Lett.* **129**, 043001 (2022).
35. H. Böckmann, S. Liu, M. Müller, A. Hammud, M. Wolf, T. Kumagai, Near-field manipulation in a scanning tunneling microscope junction with plasmonic fabry-Pérot tips. *Nano Lett.* **19**, 3597–3602 (2019).
36. S. Liu, M. Müller, Y. Sun, I. Hamada, A. Hammud, M. Wolf, T. Kumagai, Resolving the correlation between tip-enhanced resonance Raman scattering and local electronic states with 1 nm resolution. *Nano Lett.* **19**, 5725–5731 (2019).
37. B. Schröder, O. Bunjes, L. Wimmer, K. Kaiser, G. A. Traeger, T. Kotzott, C. Ropers, M. Wenderoth, Controlling photocurrent channels in scanning tunneling microscopy. *New J. Phys.* **22**, 033047 (2020).
38. A. W. Dweydari, C. H. B. Mee, Work function measurements on (100) and (110) surfaces of silver. *Phys. Stat. Sol.* **27**, 223–230 (1975).
39. B. Lamprecht, J. R. Krenn, A. Leitner, F. R. Aussenegg, Resonant and off-resonant light-driven plasmons in metal nanoparticles studied by femtosecond-resolution third-harmonic generation. *Phys. Rev. Lett.* **83**, 4421–4424 (1999).
40. R. Mittal, R. Glenn, I. Saytashev, V. V. Lozovoy, M. Dantus, Femtosecond nanoplasmonic dephasing of individual silver nanoparticles and small clusters. *J. Phys. Chem. Lett.* **6**, 1638–1644 (2015).
41. M. Merschdorf, C. Kennerknecht, W. Pfeiffer, Collective and single-particle dynamics in time-resolved two-photon photoemission. *Phys. Rev. B* **70**, 193401 (2004).
42. T. Kumagai, S. Liu, A. Shiotari, D. Baugh, S. Shaikhutdinov, M. Wolf, Local electronic structure, work function, and line defect dynamics of ultrathin epitaxial ZnO layers on a Ag(111) surface. *J. Phys. Condens. Matter* **28**, 494003 (2016).
43. C. Peng, G. Qin, L. Zhang, G. Zhang, C. Wang, Y. Yan, Y. Wang, M. Hu, Dependence of phonon transport properties with stacking thickness in layered ZnO. *J. Phys. D Appl. Phys.* **51**, 315303 (2018).
44. T. K. Cheng, J. Vidal, H. J. Zeiger, G. Dresselhaus, M. S. Dresselhaus, E. P. Ippen, Mechanism for displacive excitation of coherent phonons in Sb, Bi, Te, and Ti_2O_3. *Appl. Phys. Lett.* **59**, 1923–1925 (1991).
45. A. V. Kuznetsov, C. J. Stanton, Theory of coherent phonon oscillations in semiconductors. *Phys. Rev. Lett.* **73**, 3243–3246 (1994).
46. H. J. Zeiger, J. Vidal, T. K. Cheng, E. P. Ippen, G. Dresselhaus, M. S. Dresselhaus, Theory for displacive excitation of coherent phonons. *Phys. Rev. B* **45**, 768–778 (1992).
47. G. A. Garrett, T. F. Albrecht, J. F. Whitaker, R. Merlin, Coherent THz phonons driven by light pulses and the Sb problem: What is the mechanism? *Phys. Rev. Lett.* **77**, 3661–3664 (1996).
48. T. E. Stevens, J. Kuhl, R. Merlin, Coherent phonon generation and the two stimulated Raman tensors. *Phys. Rev. B* **65**, 144304 (2002).
49. D. M. Riffe, A. J. Sabbah, Coherent excitation of the optic phonon in Si: Transiently stimulated Raman scattering with a finite-lifetime electronic excitation. *Phys. Rev. B* **76**, 085207 (2007).
50. E. M. Bothschafter, A. Paarmann, E. S. Zijlstra, N. Karpowicz, M. E. Garcia, R. Kienberger, R. Ernstorfer, Ultrafast evolution of the excited-state potential energy surface of TiO_2 single crystals induced by carrier cooling. *Phys. Rev. Lett.* **110**, 067402 (2013).
51. J. Mertens, M.-E. Kleemann, R. Chikkaraddy, P. Narang, J. J. Baumberg, How light is emitted by plasmonic metals. *Nano Lett.* **17**, 2568–2574 (2017).

52. S. Liu, A. Hammud, M. Wolf, T. Kumagai, Anti-stokes light scattering mediated by electron transfer across a biased plasmonic nanojunction. *ACS Photonics* **8**, 2610–2617 (2021).
53. S. Liu, B. Cirera, Y. Sun, I. Hamada, M. Müller, A. Hammud, M. Wolf, T. Kumagai, Dramatic enhancement of tip-enhanced raman scattering mediated by atomic point contact formation. *Nano Lett.* **20**, 5879–5884 (2020).
54. M. Urbieta, M. Barbry, Y. Zhang, P. Koval, D. Sánchez-Portal, N. Zabala, J. Aizpurua, Atomic-scale lightning rod effect in plasmonic picocavities: A classical view to a quantum effect. *ACS Nano* **12** (1), 585–595 (2018).
55. W. Zhu, R. Esteban, A. G. Borisov, J. J. Baumberg, P. Nordlander, H. J. Lezec, J. Aizpurua, K. B. Crozier, Quantum mechanical effects in plasmonic structures with subnanometre gaps. *Nat. Commun.* **7**, 11495 (2016).
56. S. Liu, A. Shiotari, D. Baugh, M. Wolf, T. Kumagai, Enhanced resolution imaging of ultrathin ZnO layers on Ag(111) by multiple hydrogen molecules in a scanning tunneling microscope junction. *Phys. Rev. B* **97**, 195417 (2018).
57. M. Bonn, C. Hess, M. Wolf, The dynamics of vibrational excitations on surfaces: CO on Ru(001). *J. Chem. Phys.* **115**, 7725–7735 (2001).
58. B. N. J. Persson, M. Persson, Vibrational lifetime for CO adsorbed on Cu(100). *Solid State Commun.* **36**, 175–179 (1980).
59. B. N. J. Persson, R. Ryberg, Brownian motion and vibrational phase relaxation at surfaces: CO on Ni(111). *Phys. Rev. B* **32**, 3586–3596 (1985).
60. K. Watanabe, N. Takagi, Y. Matsumoto, Direct time-domain observation of ultrafast dephasing in adsorbate-substrate vibration under the influence of a hot electron bath: Cs adatoms on Pt(111). *Phys. Rev. Lett.* **92**, 057401 (2004).
61. I. Lončarić, M. Alducin, J. I. Juaristi, D. Novko, CO stretch vibration lives long on Au(111). *J. Phys. Chem. Lett.* **10**, 1043–1047 (2019).
62. J. J. Baumberg, Picocavities: A primer. *Nano Lett.* **22**, 5859–5865 (2012).
63. J. Lee, K. T. Crampton, N. Tallarida, V. A. Apkarian, Visualizing vibrational normal modes of a single molecule with atomically confined light. *Nature* **568**, 78–82 (2019).
64. Y. Zhang, B. Yang, A. Ghafoor, Y. Zhang, Y.-F. Zhang, R.-P. Wang, J.-L. Yang, Y. Luo, Z.-C. Dong, J. G. Hou, Visually constructing the chemical structure of a single molecule by scanning raman picoscopy. *Natl. Sci. Rev.* **6**, 1169–1175 (2019).
65. A. Shiotari, B.-H. Liu, S. Jaekel, L. Grill, S. Shaikhutdinov, H.-J. Freund, M. Wolf, T. Kumagai, Local characterization of ultrathin ZnO layers on Ag(111) by scanning tunneling microscopy and atomic force microscopy. *J. Phys. Chem. C* **118**, 27428–27435 (2014).
66. P. E. Blöchl, Projector augmented-wave method. *Phys. Rev. B* **50**, 17953–17979 (1994).
67. G. Kresse, J. Furthmüller, Efficient iterative schemes for *ab initio* total-energy calculations using a plane-wave basis set. *Phys. Rev. B* **54**, 11169–11186 (1996).
68. G. Kresse, J. Furthmüller, Efficiency of *ab-initio* total energy calculations for metals and semiconductors using a plane-wave basis set. *Comput. Mater. Sci.* **6**, 15–50 (1996).
69. J. P. Perdew, K. Burke, M. Ernzerhof, Generalized gradient approximation made simple. *Phys. Rev. Lett.* **77**, 3865–3868 (1996).

Acknowledgments: We thank D. Wegkamp for technical support, and Y. Sun, A. Paarmann, and S. Mährlein for valuable discussions. We thank R. Schlögl for supporting the development and preparation of the FIB tips. **Funding:** T.K. acknowledges the support by JST FOREST Program (grant number JPMJFR201J, Japan) and the Grants-in-Aid for Scientific Research (JSPS KAKENHI grant number 19 K24684) from the Ministry of Education, Culture, Sports, Science, and Technology of Japan. **Author contributions:** S.L., T.K., and M.M. conceived the experiment and performed the measurements. S.L. and T.K. performed the data analysis. A.H. prepared the Ag tip. S.L., T.K., and M.M. wrote the manuscript. All authors were involved in the discussion and commented on the manuscript. **Competing interests:** The authors declare that they have no competing interests. **Data and materials availability:** All data needed to evaluate the conclusions in the paper are present in the paper and/or the Supplementary Materials.

Submitted 15 May 2022
Accepted 2 September 2022
Published 21 October 2022
10.1126/sciadv.abq5682

ScienceAdvances

Nanoscale coherent phonon spectroscopy

Shuyi LiuAdnan HammudIkutaro HamadaMartin WolfMelanie MüllerTakashi Kumagai

Sci. Adv., 8 (42), eabq5682. • DOI: 10.1126/sciadv.abq5682

Science Advances (ISSN) is published by the American Association for the Advancement of Science. 1200 New York Avenue NW, Washington, DC 20005. The title *Science Advances* is a registered trademark of AAAS.